Malaysian Journal of Chemistry, 2025, Vol. 27(1), 242-255
(Special Issue: *International Conference in Organic Synthesis, ICOS 2024*)

Influence of Post-annealing Temperature on the Structural, Morphology, Optical and Electrical Properties of Cesium Bismuth Iodide ($Cs_3Bi_2I_9$) Perovskite Solar Cells (PeSCs) Through the Hot Immersion Method

Achoi, M. F.[1,2]*, Zulkeflee, M. H.[2], Kato, S.[2], Kishi, N.[2] and Soga, T.[2]
[1]Faculty of Applied Sciences, Universiti Teknologi MARA, Cawangan Sabah, Kampus Kota Kinabalu, 88997 Kota Kinabalu, Sabah, Malaysia
[2]Deparment of Electrical and Mechanical Engineering, Nagoya Institute of Technology, Showa-ku, 466-8555 Aichi, Nagoya, Japan
*Corresponding author (e-mail: mohdf484@uitm.edu.my)

In this paper, the influence of post-annealing on the properties of cesium bismuth iodide ($Cs_3Bi_2I_9$-CBI) perovskite solar cells (PeSCs) fabricated through the hot immersion method (HIM) is reported. Recently, lead (Pb)-based PeSCs were widely discovered, however, they are toxic material, while the CBI-based PeSCs are a non-toxic material. The CBI fabricated using a simple method by changing the post-annealing temperature (PAT) between 100ºC and 250ºC. The XRD results showed that the crystallinity of the CBI film was improved, and crystallite sizes were increased as well, which is from 20 nm to 23 nm at 100ºC and 200ºC, respectively, while the surface morphology showed that the island-like structure and compact surface. On increasing the PAT, an increase in the average surface roughness from 355 µm to 1,016 µm was observed, due to the enlargement of CBI crystal structure under continuously applied heat and PAT. The increment led to an enhancement of the optical properties with a narrower indirect bandgap, which is from 1.92 eV to 1.89 eV to 1.86 eV to 1.87 eV at 100ºC, 150ºC, 200ºC and 250ºC, respectively. Eventually, the performance of HIM-fabricated CBI-PeSCs showed an increment, particularly the short-circuit current density (J_{sc}), which is one thousand eight hundredfold increases, i.e., from 2.5 x 10^{-4} mA/cm^2 to 0.45 mA/cm^2 at 200ºC. It thus gives the potential impact as it will help contributing to the body of knowledge of solar cell development with stable and non-toxic PeSCs. Our findings give useful new knowledge for the fabrication of CBI PeSCs through a simple method with a non-toxic material, and it could be a useful approach in the development of Pb-free PeSCs in the future work.

Keywords: CBI; perovskite; solar-cells; hot-immersion method; post-annealing

Received: September 2024; Accepted: December 2024

To date, lead (Pb)-based perovskite solar cells (PeSCs) have been attracted much attention by previous researchers due to its outstanding properties such as high efficiency and a better performance of PeSCs [1]. However, Pb-PeSCs have a low stability in ambient air and a toxic material [2, 3]. Moreover, the Pb-PeScs has debuted and confronted its current problem, resulting in limitation of its commercialization up to now. Therefore, the right candidate to replacing the Pb-PeSCs is necessary. Among them are Bismuth (Bi)-based perovskite and Cesium (Cs)-based perovskite. For Bi-based perovskite, bismuth is a non-toxic material [4] and having a stable element [5], which leads to stable $6s^2$ valence electrons. Moreover, the Bi-PeSCs has a similar electron configuration compared to Pb^{2+}. However, their performance is low at present [6, 7, 8] due to poor morphology [9, 10] especially the current density [2]. In addition, the absorption wavelength region towards a longer wavelength region and optical bandgap are shorter and wide, respectively, than CBI-PeSCs [11]. For example, B.M. Bresolin et al. found $(CH_3NH_3)_3Bi_2I_9$ has absorption band-edge wavelength region is around 550 nm by MA gas deposition [12]. A. Mutlu et al. reported on the high quality MBI-based perovskite solar cells has a wavelength region is less than 560 nm [13], while T. Mohammad et al. found the absorption band-edge region is around 570 nm by electric field spray coating [11]. Correspondingly, the MBI has a wide direct bandgap energy which is around 2.10 eV [14]. While, for CBI-PeSCs is the right candidate to replacing the Pb-based PeSCs due to non-toxic materials [3, 15], and excellent thermal stability [16]. Hence, it is right candidate to replacing Bi-PeSCs as well [17], and it has similar structure with bismuth, which has a bioctahedral structure that shares the face of binuclear $(Bi_2I_9)^{3-}$ and then surrounded by Cs^+ cations [18]. The advantages of Cs-based perovskite than Bi-based perovskite is Cesium cation has a smaller ionic radius compared to methylammonium (MA^{+}) as reported by I. Borriello et al. [19]. In addition, the

†Paper presented at the International Conference in Organic Synthesis 2024 (ICOS 2024)

bandgap of CBI is smaller than that of MBI [6, 20], which has a smaller indirect bandgap of 1.90 eV and it thus has a better in light absorption as reported by Z. Qi et al. [21]. S. Aiba et al. reported that Cs^+ cation has improved the light absorption of the perovskite solar cells [22]. Therefore, the selection of Cesium to be replaced with the methylammonium bismuth iodide owing to its excellent UV-absorption of light properties, has a smaller ionic radius and a narrow bandgap, and good stability is a suitable candidate. Hence, in this study, we choose the CBI-based perovskite to fabricate the perovskite solar cell and replace the lead-based perovskite solar cells and Bi-PeSCs. However, the CBI perovskite is still suffered a problem with poor surface morphology [10, 20] due to hexagonal structure and a large crystal structure. Therefore, in this study, our aim is to improve the CBI film morphology by using a simple method that will be briefly discussed in the next two paragraphs.

On the other hand, the method of fabrication of CBI-PeSCs is important because it determines the quality of a perovskite film being produced. In addition, it influences the performance of perovskite solar cells due to absorber active layer relying on the method of fabrication [23, 24]. Recently, the perovskite solar cells particularly Pb-PeSCs and Bi-PeSCs are often prepared by spin-coating method to obtain high-crystalline and pinhole-free film. However, spin-coating is required of nitrogen gas during the fabrication process, and it is not a simple method due to controlling of a few parameters such as controls of the spinning rate and the time of coating [16, 25]. Moreover, it is waste of precursor solution and is necessary to perform inside the glove box. Other method involved in fabricating of CBI-PeCS that required technical handling and controlling parameters is spray coating [26, 27], dripping of solvent [22], vacuum-assisted thermal annealing [28], chemical vapor deposition [29], MA gas deposition [13] and others. All those methods are still suffering problems with the CBI morphological, particularly the performance of CBI-PeSCs is still low at present. The highest ever recorded efficiency for CBI-based perovskite solar cells is 3.2% in 2023 [16].

Therefore, in this study, we have used a simple method in preparing compact films [30, 31] and consumption of precursors is less, and it does not require technical handling such as those method mentioned above, namely as hot immersion method (HIM). Thus, it suggests that the possibility of fabricating perovskite solar cells at a low cost. In addition, this technique is a promising and effective method to achieve high-crystallinity film and good morphology of perovskite film. This method has been well-proven and consistently fabricated the perovskite film with a better morphology and a high crystallinity of perovskite according to our previously reported work [2, 32]. In comparison with the spin-coating in terms of achievable film quality, cost and scalability, the similarity of produced films is almost similar. However, HIM does not employ gas, pump machines and related spin appliances, instead spin-coating uses all those mentioned. It thus making spin-coating is more expensive than HIM. In addition, HIM offers flexibility of fabrication due to wide space of immersion deposition for film, while spin-coating is limited space and needs to be performed inside the glove box through a provided small stage, yet both approaches still producing a good quality of film. Herein, the influence of post-annealing temperature on the properties of CBI-PeSCs and its performance are evaluated. As far as our concern, the effect of this parameter on crystalline, morphology, and the optical properties of CBI film has not been reported elsewhere, particularly using this method. Correspondingly, the knowledge gap in respect of CBI performance is the different methods that have been employed, yet the quality of film is still achievable through simple and low-cost approaches. Moreover, the electronics properties of the film are attainable.

By optimizing the influence of post-annealing temperature, the CBI films with high crystallinity, a narrowed bandgap at extended wavelength bandgap-edged absorption region and compact morphology that fabricated by a simple method can be successfully achieved and enhanced. As a result, the electronic properties, particularly the current density have been enhanced, thereby, the performance of CBI perovskite solar cells is still attainable even though the performance is still low at present. Additionally, we managed to improve the surface morphology and optical bandgap of CBI-PeSCs than our previous reported work [22] in last year that using spin-coating and anti-solvents.

EXPERIMENTAL

Preparation of Substrate, CBI, ETL and HTL

Firstly, the Fluorine Tin Oxide (FTO) glass with a dimension of 2 cm x 2 cm was selected as an electrode substrate. The FTO glass was cleaned with acetone and ethanol solution, two times each of them, respectively, to ensure the cleanliness of the substrate. Then dried under nitrogen gas blowing. Next, the preparation of compact titanium dioxide /mesoporous titanium dioxide (c-TiO_2/mp-TiO_2) as an Electron Transport Layer (ETL) and CBI film were prepared, and they fabrication process have already been discussed in our previously reported work [7, 33]. In brief, both precursors of Cesium Iodide (CsI) powder and bismuth triiodide (BiI_3) powder (purchased from Sigma-Aldrich, 99%) were mixed in a 10 mL solvent of dimethyl formamide [$HCON(CH_3)_2$] (DMF) with ratio [1.5:1.0] to form a 0.5 M CBI solution. The mixture was then stirred continuously until it was resolved completely, and it left for aging time, and followed by hot immersed on the mp-TiO_2/c-TiO_2/FTO/ glass. For this purpose, the TiO_2 coated FTO glass was immersed in the mixture of both precursor solutions at 30°C for 18 h as shown in inset Figure 7(i). Next, the sample was annealed at 100°C for 10 min and left for cooling at room

temperature for about 10 min. The samples were then post-annealed at 100ºC, 150ºC, 200ºC, and 250ºC for 60 sec and again left for cooling at room temperature. The rationale of selection of these temperature ranges was considered ideal to investigate the effect of PAT on the properties of CBI and to prevent degradation of the CBI film at high PAT, while at lower temperature, the film is insufficient to crystallize and attributed to the existence of pinhole. G.E. Eperon et al. reported that the film might degrade at high annealing temperature and cause the quality of a film to become poor [49]. While the reason for selection of hot immersion temperature at 30ºC is to ensure the immersion solution does not evaporate at high temperature. According to O. Shargaieva et al., high temperatures may cause the evaporation of the solution [39]. Moreover, HIM is still a new approach that introduced by our research group [31] and has no report elsewhere particularly for immersion temperature. Finally, the preparation of poly(3-hexylthiophene-2,5-diyl) (P3HT) as a Hole Transport Layer (HTL) was followed as reported earlier [7]. In brief, P3HT powder was dissolved in dichlorobenzene to make 15 $mg.mL^{-1}$ of P3HT. The prepared P3HT solution was then spin-coated at 3000 rpm for 20 s and then annealed on a hot plate at 120ºC for 15 min. The entire process of fabrication was carried out in a glove box under a flow of nitrogen gas. Note that the fabrication of CBI films was fabricated three samples for each of PAT (100ºC, 150ºC, 200ºC and 250ºC) to confirm the reproducibility of the sample.

Fabrication of CBI Solar Cell Device

All the prepared solutions in the previous step were used for the fabrication process. First, as a final step of preparing the CBI cells, an insulator tape (Nichiban polymer brand) was punched to make a hole by a puncher and then the tape is carefully displayed on top of the HTL layer (P3HT) by using forceps. The punched hole size was 3 mm in the middle of the tape (hole for the carbon and silver paste). The active area was around 0.071 cm^2. Next, the carbon solution as an electrode was prepared according to ref. [32], and in the active area, the prepared carbon was deposited by spin coating at 5000 rpm for 20 sec, and followed by silver paste on the top carbon layer was placed in a small amount by using a dropper. Finally, both layers (carbon and silver paste) were dried at room temperature for 5 min. The purpose of using the carbon was to provide a better connection between the connector (Ag paste) and the entire MBI cell structure [34] as shown in inset Figure 7(i).

Characterization of CBI film

The structural and morphology of CBI films were characterized by X-ray diffraction (XRD; Rigaku RINT-2100 diffractometer) and scanning electron microscopy (SEM; JEOL JSM 7600F), respectively. For the XRD, the X-ray radiation source of Ni-filtered Cu Kα radiation with wavelength, λ = 1.5408 Å and equipped with a Cu target was used (Rigaku Smartlab). The UV-absorption properties and the surface roughness of the films were characterized using a UV-Vis spectrophotometer (JASCO Model V-570) and the Dectak machine (Veeco-Dektak 150), respectively.

The CBI Solar Cell Measurement

The CBI Cells were evaluated by the current-voltage (I-V) measurement under a solar simulator that is equipped with a Xenon lamp (model PS-X500) and measured by using a 238 Keithley high current source. In addition, the simulator was configured with white light illumination at AM 1.5 and 100 $mW.cm^{-2}$ of class AA spectra, while the voltage interval used was 0.01V with a scan rate of 50 mV/s and import condition DC setting with N/P polarity.

RESULTS AND DISCUSSION

Structural Properties

Figure 1 shows the XRD curves of CBI films with post-annealing at different temperatures. All the CBI peaks are indexed as a hexagonal structure with space group $P6_3/mmc$ (ICDD card data no. 04-008-8708) [2]. In general, all the CBI peaks are typically assigned to 12.82º, 25.86º, 27.5º, 29.68º, 32.40º and 42.99º, which correspond to (101), (202), (203), (204), (205), and (220) lattice planes, respectively [2]. Other CBI peaks are observed at diffraction angles of 21.22º (110) and 45.79º (209) [15]. All these peaks are the same as reported [2, 22]. At the beginning, post-annealing temperature of 100ºC, it can be observed that all the CBI peaks exhibited as sharp peaks with high in intensity, particularly at 25.86º (202), 27.54º (203) and 29.68º (204). However, the CBI peaks at 21.22º (110), 25.86º (202), 32.40º (205) and 42.99º (220) appeared as a low intensity peak, as can be observed in Figure 1a. Additionally, peak at 25.86º (202) appeared lower than peak at 27.5º (203). On increasing the PAT to 150ºC, these four peaks gradually increased, while the other peaks remain as seen earlier. It means the crystallinity of CBI films has improved. On prolonging the PAT to 200ºC, interestingly the peak at 25.86º (202) has now appeared dominantly with a very strong, intense and a narrow peak than CBI peak at 27.54º (203) and 29.68º (204). In addition, the peak at 25.86º (202) as seen before appeared as a low intensity, and now seen appeared higher than peak at 27.5º (203), which indicates that the temperature influence the crystallinity of CBI film, particularly the CBI peaks at 21.22º and 42.92º became a bit high intensity compared as seen earlier, as shown in Figure 1c, proving that the crystallinity of CBI film is being further enhanced. However, at maximum of post-annealing temperature, 250ºC, the formation of CBI hexagonal structure was distracted due to much evaporation of the solvent after further annealing applied on the annealed CBI film at 100ºC of pre-annealing, as shown in Figure 1d. This happened due to high heat being imposed into the CBI film at 250ºC

of post-annealing, as a result, the film degraded and left an empty space as shown in Figure 4d. In brief, the crystallinity of CBI films increased from 100°C to 200°C, however, at high temperatures, the CBI film starts to degrade due to evaporation of the solvents, which will be further discussed in Figure 3 and Figure 4. According to Md. Shahiduzzaman et al. $Cs_3Bi_2I_9$ perovskites starts to be vaporized at 220°C of annealing temperature [28].

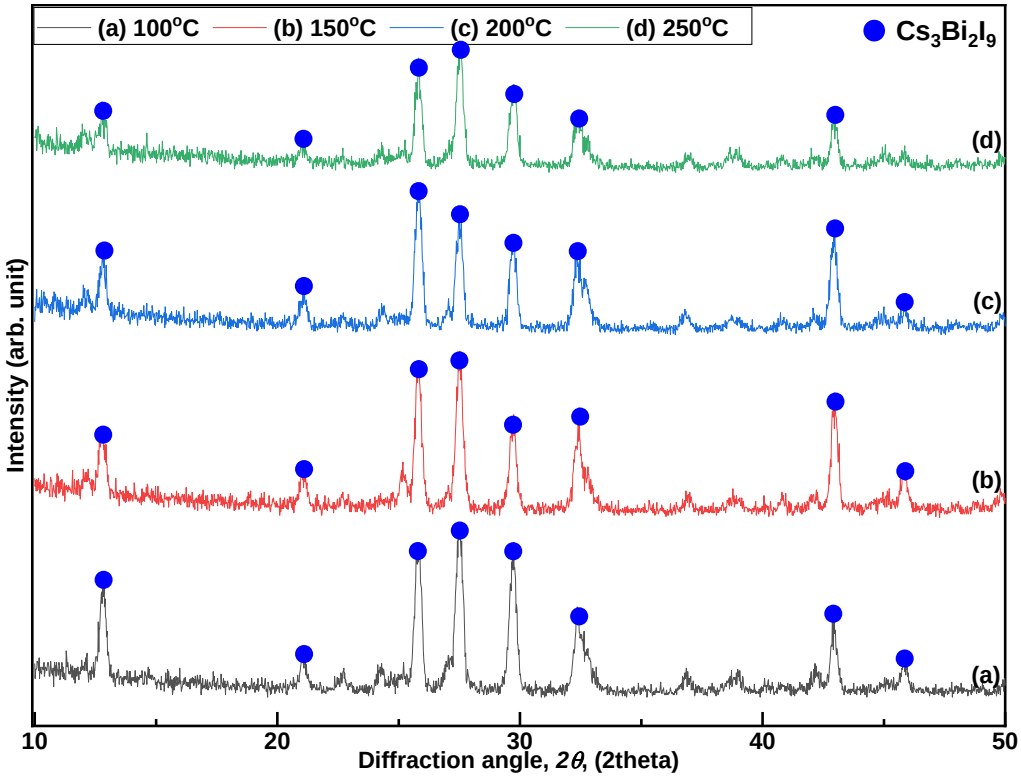

Figure 1. XRD curves of CBI films at different post-annealing temperatures, T_{pt}: (a) 100°C, (b) 150°C, (c) 200°C, and (d) 250°C.

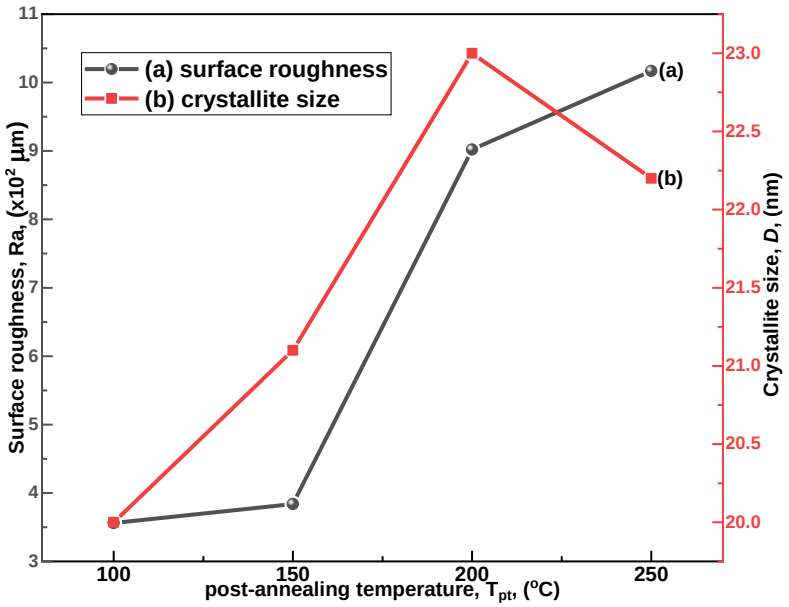

Figure 2. Surface roughness and the crystallite size of CBI films as a function of the post-annealing temperature.

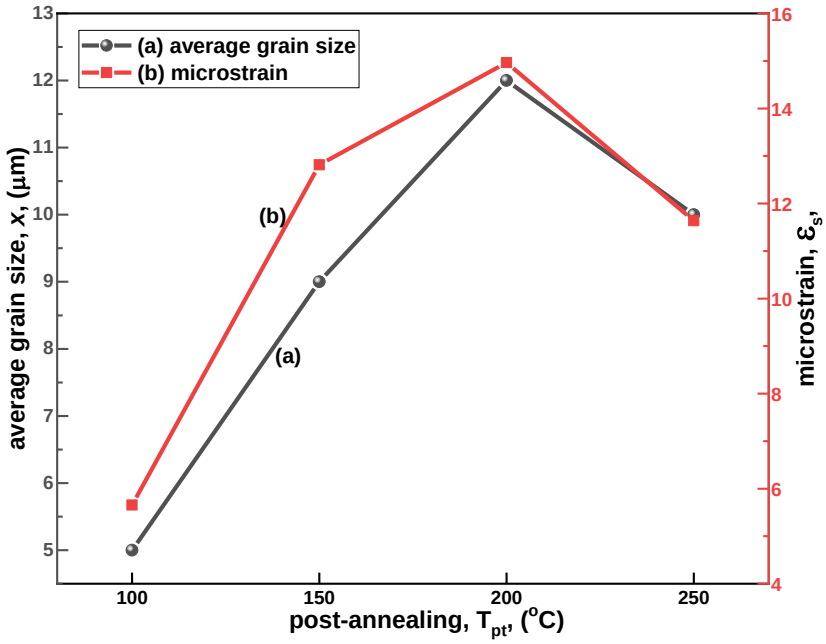

Figure 3. (a) average grain size, <x>, of post-annealed samples as a function of temperature (T_{pt}) obtained from top-view SEM images (ImageJ software), and (b) is the microstrain of the CBI films.

In this connection, increasing the PAT contributed to the increment of surface roughness in Figure 2a. Similarly to the CBI crystallite size, *D*, showing an increment as well, from 100ºC to 200ºC, except for post-annealing temperature at 250ºC, as can be seen in Figure 2b. This might be due to the evaporation of solvent causing the film is being degraded, as mentioned earlier, resulting in a bit small crystallite size, *D*, than *D* at PAT of 200ºC, as a proof, in Figure 1d, at 250ºC, peak at 12.82º (101), 32.40º (205) and 42.92º (220) were appeared a broad and low intensity peak, particularly peak at 45.79º were disappeared indicating that the crystallinity of CBI film become a very poor. It is expected that it will influence the film surface morphology, which will be discussed in the SEM section. While, on increasing of PAT from 100ºC to 200ºC, attributed to the increment of *Ra* and *D*, as can be observed in Figure 2 due to the induction of high temperature onto the film during the post-annealing process, while *Ra* and *D* values are small since less nucleation and crystallization [10] occurred at a low temperature. It can be observed that the crystallite size was a little increment, which was increased from 20.0 nm to 21.1 nm to 23.0 nm, as compared to surface roughness, which was increased from 3.55 x 10^2 µm to 10.16 x 10^2 µm. We notice that the difference increment value of both parameters was much different due to the reaction temperature having much effect on the film surface than the crystallite size, similarly to the grain size, which will be discussed further on the next paragraph. In brief, this happened due to the crystallization growth effect [10] on the CBI crystal structure led to larger grain size. Consequently, the grain size increases with the post-annealing temperature due to congregation effect [35]. Our explanation is in agreement with the reports of Clabel et al. [36]. In brief, both parameters increased accordingly, because of the increasing the post-annealing temperature from 100ºC to 200ºC. The crystallite size and surface roughness values of CBI films are tabulated in Table 1.

Furthermore, as discussed earlier, the reaction temperature has much effect on the surface roughness of CBI films, same as the grain size, which was increased from 5 µm to 12 µm as increasing the PAT from 100ºC to 200ºC, as shown in Figure 2(a) and 3(a), respectively. It is well known that the CBI has a hexagonal shape and crystal structure [10, 15], thus the imposed heat temperature causing the CBI crystal structure grew largely due to crystallization and quick nucleation process [2, 10] and sank with overlapped to each other resulting in the increases of microstrain of CBI film at high post-annealing temperature, as shown in Figure 3b, which was increased from 5.655 to 14.964 before the film experience failure (degradation), as discussed earlier. It means the film strain is 14.964 in maximum strain at post-annealing temperature of 200ºC and then deform with strain of 11.638 at 250ºC, as shown in Figure 3(b). Similarly to the grain size in Figure 3(a), shows the increment before deforms at 250ºC, that will be further discussed in SEM section. This indicates that the CBI film sustains at maximum strain (ε_{max}) from proportional limit (at the beginning of PAT) of the film before underwent a failure and become a small grain size. This failure is attributed to the deformation of film morphology and resulting in the decrement of porosity and film density that will be discussed further in the next SEM section. The strain is the failure (defect) or change of structural properties of the film that happened during the post-annealing. These results

suggest a dependence of the microstrain of the film on the PAT. The microstrain of the CBI film was calculated using equation 1 [37, 38] and its value is tabulated in Table 1:

$$\varepsilon_s = \frac{\beta \cos\theta}{4} \quad (1)$$

Where ε_s is the microstrain of the film, β is the full width at half maximum (FWHM) and θ is the Bragg angle. This result is in line with the *D* result which showed an increment before deforming at 250°C that is discussed earlier in the XRD section. In brief, the microstrain of the CBI film is much affected by PAT, whereby the value of the strain is between 5 and 15 for all the samples, and at the same time, the average grain size values are increased as well, as can be seen in Figure 3a and 3b, respectively. Our results agree well with the reports of Md. Shahiduzzaman et al. who found that the perovskite crystal sizes were larger at 160°C and above, then vaporized [28].

Surface Morphology Properties

Figure 4 shows the SEM morphologies of the CBI films at different post-annealing temperatures, while the graph of film porosity and density as a function of T_{pt} is shown in Figure 5a and 5b, respectively. The grain size of CBI was performed in a similar way as reported by Shargaieva et al. [39] as shown in Figure 3a. In brief, the grain size calculation was performed from the top-view SEM images with ImageJ software [37]. In the same manner, from the SEM images, the percentage of porosity (via ImageJ software) was calculated for the CBI film [40], as shown in Figure 5a. At 100°C post-annealing temperature, it can be observed that a longer needle-like structure (white color and orange color circle) with a small island-like structure (blue color) of CBI are randomly distributed with each other, as can be seen in Figure 4(a), while the average grain size of those structure is around 5 µm in Figure 3a and surface roughness, *Ra*, is 3.55 x 10^2 µm. However, these needle-like structures (orange color circle) with a small island-like structure are gradually grown with the average grain size of around 9 µm at a post-annealing temperature of 150°C, as shown in Figure 3a, while *Ra*, is 3.384 x 10^2 µm. This time the needle-like structure as seen earlier is growing larger with some needle disappearing, and the small island-like structure (blue color) as seen before is now clearly seen with grow largely and dominant, yet still distributed randomly same as seen earlier. In addition, as seen before, the wide space left between those structures, and now it is seen close to each other with the gap between the structures becoming closer than earlier, as can be seen in Figure 4b. On increasing further the post-annealing temperature to 200°C, surprisingly observed that the film morphology was absolutely changed than earlier seen in which the film is now become flat and compact surface with no empty space left, and this time the average grain size is 12 µm as shown in Figure 3a and Figure 4c, while *Ra*, is 9.02 x 10^2 µm. It means the island-like structure that seen earlier grew largely, and then sank to each other, resulted in a continuous surface, compact of film and present grain boundaries in red color as shown in Figure 4(c). In addition, the surface is dense and compact with composed of large crystals structure of CBI that sank with overlapping to each other. This mechanism of the CBI formation has been reported in detail in our previous reported paper [2]. Moreover, this happened due to quick nucleation [41] and high crystallization process upon applying heat, as reported by C. Lan et al. [42]. Finally, at 250°C of post-annealing temperature, the CBI formed continuous film, compact and flat surface as seen before, and now being degraded due to failure and deformation of a film as discussed earlier in XRD section in Figure 3(b) and might be due to the applied high temperature either, as shown in Figure 4d. This also influences the average grain size, microstrain and crystallite size, whereby all of them decrease after maximum T_{pt}, as shown in Figure 3 and Figure 2, respectively. In Figure 4d, it can be observed that the film morphology is degraded with leaving an empty space, which is valleys as a defect (yellow color) and this time the average grain size is 10 µm and *Ra*, is 10.16 x 10^2 µm. The reason for this change in morphology is due to the change in the crystal structure of CBI. The detailed mechanism on changing of the CBI structure has been discussed and reported in ref. [2]. In the early discussion, crystallite size increases accordingly with average grain size as increasing the T_{pt}, proving that the CBI crystallite sizes were combined and accumulated as a grain on exposure to annealing temperature, which means that the crystallite size lie under grain. Our explanation is supported by Clabel et al. who explained that the grains consist of several crystallites, which combine and led to larger grain size [10, 28]. In brief, the crystal structure of CBI increases with increasing the PAT, the CBI crystal structures grew largely under fast crystallization process and quick nucleation growth [41, 42] and then combined and sank to each other with no empty space is left, as a result the surface becomes flat, compact and rough surface as shown in Figure 4c and Figure 2a, respectively. On increasing further, the PAT causes the film to degrade and leaves a defect due to the film deformation (failure) as discussed earlier. Incidentally, we noticed that there is no hexagonal shape of CBI due to destruction of hexagonal shape as a result from two times of annealing (pre-annealing at 100°C and applied post-annealing temperature from 100°C to 250°C), and high imposed of heat temperature onto the CBI film. Eventually, the post-annealing temperature has a strong effect on the crystallite size, roughness, microstrain, and grain size of CBI film. All those parameters mentioned are expected to influence the performance of the CBI solar cell, which will be discussed in the next performance section. All surface parameters are tabulated in Table 1.

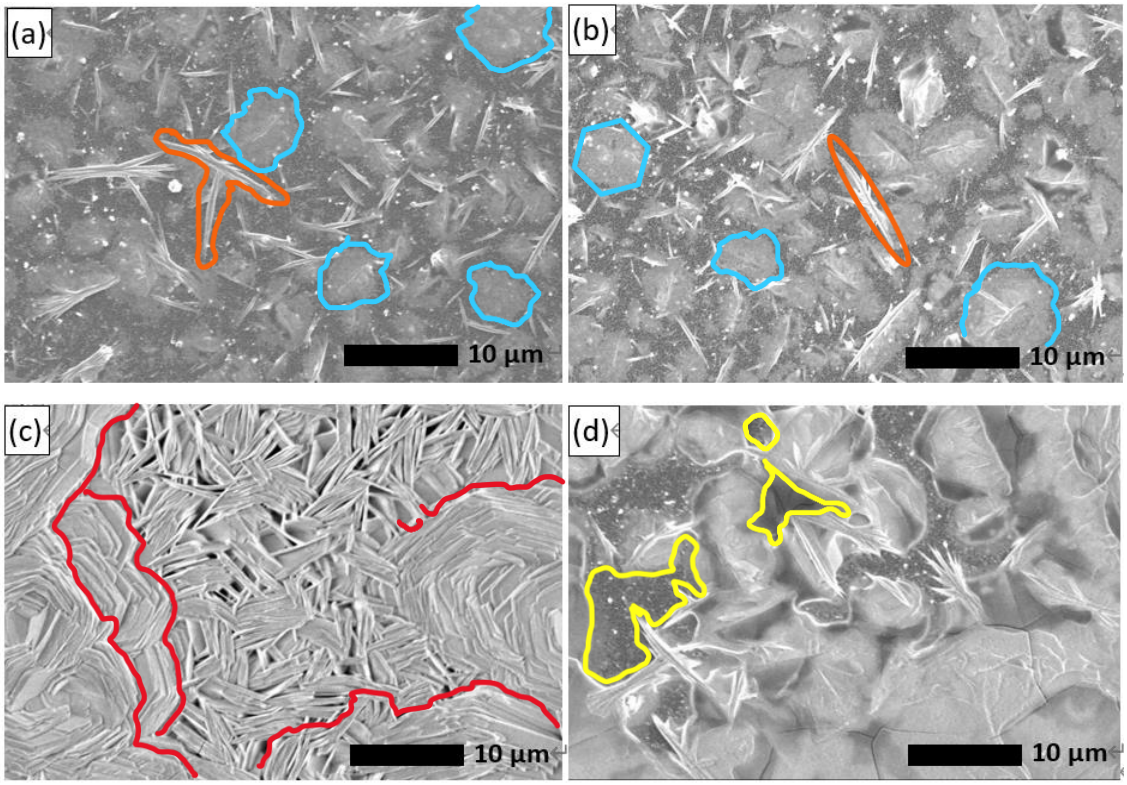

Figure 4. SEM morphology of CBI films at different post-annealing temperature, T_{pt}: (a) 100°C, (b) 150°C, (c) 200°C, and (d) 250°C.

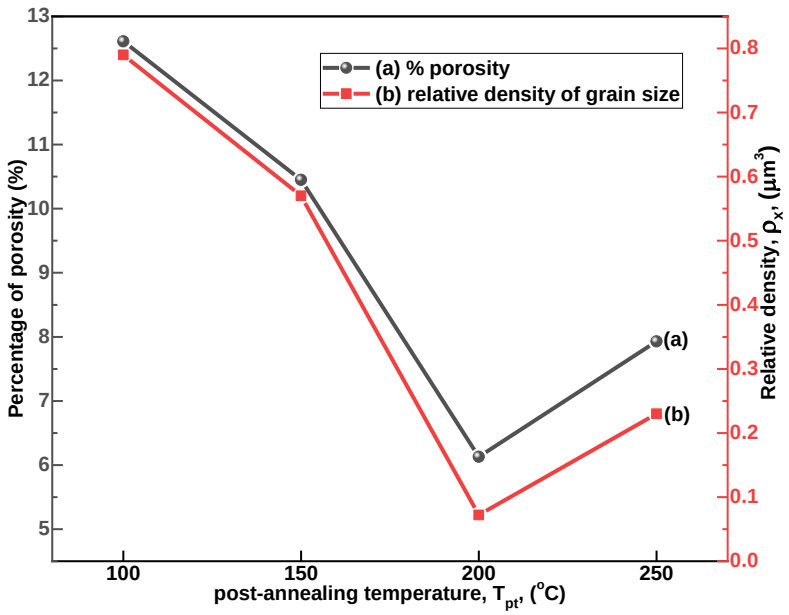

Figure 5. The variation of percentage of porosity and relative density of the CBI films against post-annealing temperature.

On the contrary, as discussed before, the CBI film porosity and density shows that the decrement trend as increasing the T_{pt} until 200°C, however, increasing again at 250°C, as shown in Figure 5. This happened due to the enlargement of grain size [28] as shown in Figure 3a, which is attributed to the reducing of film porosity from 12.61% to 6.13% as increasing the T_{pt} from 100°C to 200°C in line with the results of SEM in the previous discussion, as shown in Figure 5a. In brief, large grain size showed less porosity, while small grain size showed high porosity. Similarly, the relative density of the CBI film decreased accordingly with the porosity of the CBI film as shown in Figure 5b. To validate this, we have

performed porosity analysis through SEM image (ImageJ software) [40], while the CBI film density was calculated using equation 2 [37], and all its values are tabulated in Table 1.

$$\rho_x = \frac{n}{A} \quad (2)$$

Where ρ_x is the relative density of film, n is the number of grains in the specified area, and *A* is the area of the film that is reflected in the counted grain. We found that the increase in grain size of CBI as discussed earlier in the XRD section decreased the density and porosity of the CBI film, which attributed to reduction in the number of grains in the specified area as shown in SEM images, Figure 4a-d. Similarly, as discussed early, this happened due to post-annealing temperature and crystallization growth process [42], resulting in grain growth of CBI crystal structure which is attributed to less porosity with a decrease in density as tabulated in Table 1 and as shown in Figure 5. Eventually, it is attributed to the high crystallinity and compact morphology of CBI film as shown in Figure 1c and Figure 4c, respectively. The decrease in film porosity and density of the CBI film may influence the UV-absorption properties of CBI film, which will be discussed in the next UV-absorption sections and the performance of CBI-PeSCs section. In brief, an increment of PAT contributed to reducing porosity and film density, and the enlargement of CBI crystallite size.

Table 1. The structural parameters for the CBI thin films at different post-annealing temperatures.

T_{pt}, (°C)	*D* (nm)	*Ra*, (x10^2) (µm)	Porosity (%)	Thin film microstrain (ε_s)	Relative density, ρ_x, (μm^3)	Average grain size <x>, (µm)	Indirect bandgap (E_g), (eV)
(a) 100	20.0	3.55	12.61	5.655	0.79	5	1.92
(b) 150	21.1	3.84	10.45	12.815	0.57	9	1.89
(c) 200	23.0	9.02	6.13	14.964	0.07	12	1.86
(d) 250	22.2	10.16	7.93	11.638	0.23	10	1.87

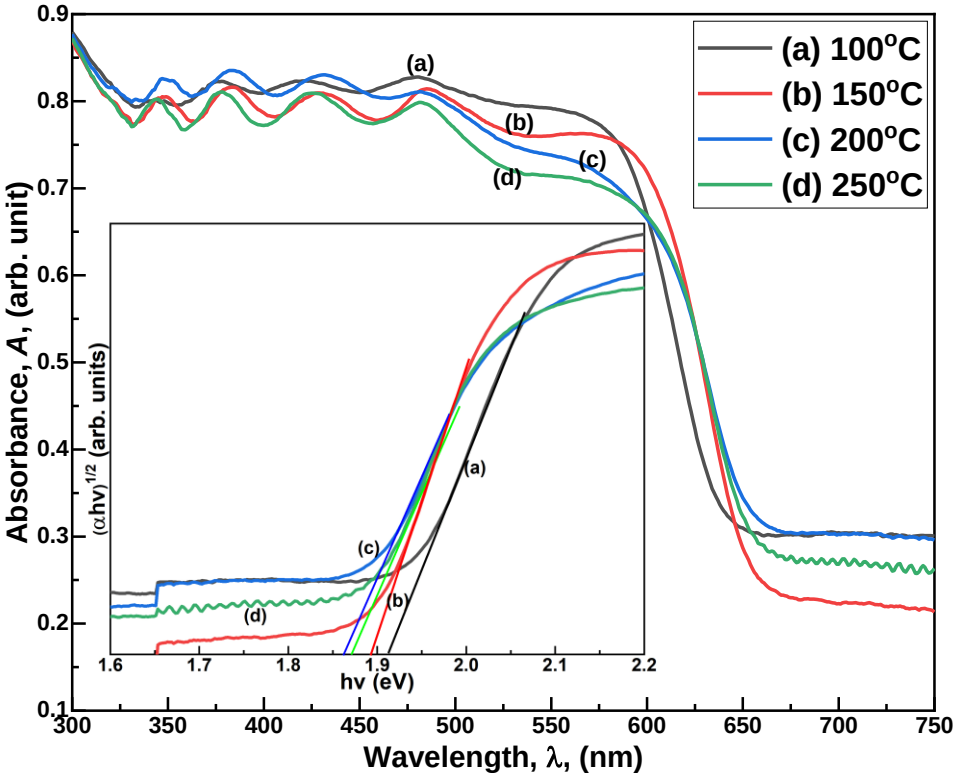

Figure 6. Optical properties of CBI-PeSCs at different post-annealing temperatures, T_{pt}: (a) 100°C, (b) 150°C, (c) 200°C, and (d) 250°C. Inset figure is Tauc's plot showing the indirect bandgap.

UV-Vis Absorption Properties

Figure 6 shows the UV absorption properties of CBI film, while the inset indicates the indirect bandgap plotted by Tauc's plot [10, 37] versus the energy of light by extrapolating a linear line absorption edge in a function of $(\alpha hv)^{1/2}$ versus = $hv(eV)$ [43]. While the UV-Vis absorption test was performed by measuring the transmittance T (λ) and reflectance R (λ) spectra of the fabricated CBI film. In our study, T (λ) and R (λ) have been recorded within the wavelength range of 300 – 750 nm. The absorbance value of CBI film has been estimated using the equation 3 [44] and the plotted graph as depicted in Figure 6.

$$(A + T + R) = 1 \quad (3)$$

Where A, T, and R denote the film's absorbance, transmittance, and reflectance, respectively. Our result is in line with reported [3]. In general, high absorbance value is mostly and consistently recorded at high value of 0.83 within wavelength region of 325 – 475 nm, for post-annealing temperature of 200°C (in Figure 6c) as compared to other T_{pt}, while the T_{pt} of 100°C and 150°C have recorded almost similar value of absorbance in between wavelength region of 300 – 500 nm, which is 0.80 – 0.81. It means that the absorbance value increased with the increase in grain size and surface roughness with less porosity of CBI film as the post-annealing temperature was increased from 100°C to 200°C. However, the CBI film post-annealed at 250°C with poor morphology and inhomogeneous film as shown in Figure 4d attributed to the low absorbance intensity after underwent deformation of film (defect) as discussed earlier in Figure 3b. In addition, the CBI film with high crystalline, compact surface and less porosity, and large D and high Ra, as shown in Figure 1c, Figure 4c, Figure 5a, Figure 2b, and Figure 2a, respectively, are attributed to high absorbance intensity around the visible region. Consequently, the CBI film at 200°C, resulting in a small indirect bandgap value which is 1.86 eV, as shown in inset Figure 6c. The reason for high absorbance intensity at T_{pt} of 200°C is due to absent defect such as porosity on the surface of film (in Figure 4c) with larger grain films and rougher surface as discussed earlier, and thus, it reduced the reflection effect on the film surface and less light scattering with a better light trap, thereby, contributed to the better absorption [37, 45]. Moreover, the absorption band-edge shoulder extended towards NIR wavelength region is around 677 nm as shown in Figure 6c. Thus, a high absorbance and consistent value in visible region were produced. It means that the CBI film is a better light harvesting in the Pb-free Cesium-based PeSCs. Our result agrees well with this finding [5, 36, 37], reported the optical bandgap is reduced while the annealing temperature was increased. It is expected that optical absorption may influence the device performance, which will be discussed in the next section. In summary, the absorbance intensity increased, and the indirect bandgap became smaller, as the post-annealing temperature increased from 100°C to 200°C.

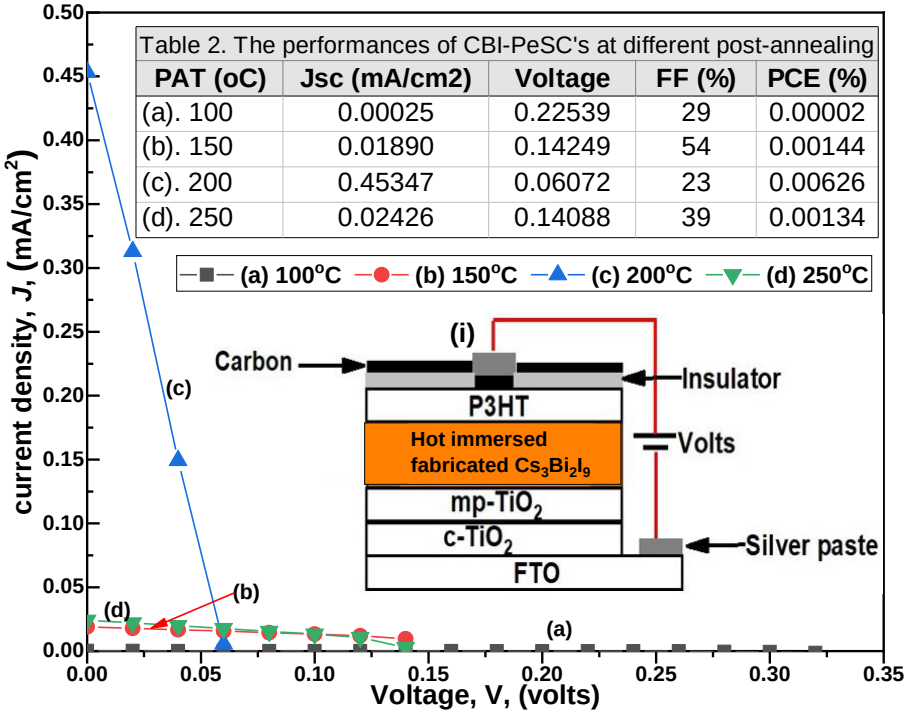

Figure 7. The CBI solar cell performance at different post-annealing temperatures, T_{pt}: (a) 100°C, (b) 150°C, (c) 200°C, and (d) 250°C.

The CBI Solar Cell Performance

Figure 7 shows the I-V curves of fabricated CBI cells at different post-annealing temperatures, whereas the solar cell parameters are summarized in inset Table 2, while its parameters graph is plotted in the Figure 8a-d, and the inset Figure 7(i) is the schematic diagram of the fabricated CBI cell structure. The measurement reading in inset Table 2 was taken three times to obtain the average of reading of all parameters, and the measurement was performed in ambient air for four samples. In general, on increasing the post-annealing temperature from 100°C to 200°C, shows that the increasing of CBI cell performance. However, it can be observed that the decrement trend of V_{oc} from 100°C to 200°C, which is from 0.23 V to 0.06 V, before increases again at 250°C as can be seen in Figure 8b. On the contrary, current density and the percentage of efficiency are showing increment trend before decreasing back at 250°C of PAT, as shown in Figure 8a and 8d, respectively. The reason of this situation happened will be discussed further on the next paragraph.

However, the fill factor shows that the fluctuating trend, particularly sample at 200°C showed only 23% of FF with a low of voltage is 0.06 V only. There are two possible reasons that might be considered. First, a low of voltage value caused by the large crystals appear with increasing PAT and the surface becomes flat. Our explanation is in line with our previous finding and the study on the CBI structure [2], which showed the lower value of voltage and high current density were recorded, with compact and dense of CBI film as compared to other sample. We found that the CBI composed of a large crystal size of CBI, and this crystal grew largely due to the nucleation growth as increasing of PAT, as a result, the crystal combined and accumulated with each other resulting in rougher and compact film, resulting in increases of the thickness of CBI film affected the produced voltage, as can be seen in Figure 4c and 8b, respectively. Our explanation is in line with the report of [22], found that the value of V_{oc} is a low as well, while the recorded value of current density is high. On the other hand, the possible reasons for the decrease in FF are the increase in series resistance occur via the additional resistance component or the decrease in parallel resistance occur via the increase in the defect density or film deformation (defect) of the perovskite film, in the equivalent circuit [2, 46].

As a proof, the V_{oc} value decrease with increasing the PAT because the saturation current J_0 increases from equation (4). Instead, the value of V_{oc} increases as the decrease in saturation current J_0, as shown in equation 4 [46]. However, due to the poor morphology as shown in Figure 4a and 4b contributed to the high leakage current of CBI films, thereby producing a low current density as shown in Figure 8(a). Instead, at 200°C of PAT producing a higher current density and efficiency, whereby 0.45 mA/cm^2 and 0.006%, respectively, as compared to others. This happened due to the rougher surface and less porosity of a film were encouraged a better absorption of light by reducing the reflection effect. It means that the sample with high porosity and less rough attributed to the current leakage and high reflection effect as can be seen in Figure 2a and Figure 5a, respectively, resulting in increased charge recombination in the cells, thereby contributing to the poor performance of the device, as shown in Figure 7d and Figure 8d. Since the power conversion efficiency is proportional to the product of J_{sc}, V_{oc}, and FF, the efficiency values gradually increase with the post-annealing temperature as shown in Figure 8d, except the sample at 250°C due to poor morphology as discussed earlier.

$$V_{oc} = \frac{kT}{q} \ln\left(\frac{J_{sc}}{J_0} + 1\right) \quad (4)$$

However, the V_{oc} increases at PAT of 100°C, 150°C and 250°C. This means that the decrease of FF is not due to the decrease in parallel resistance, however due to the increase in series resistance. The FF and the voltage increase again at 250°C, probably due to the recovery of series resistance.

The second reason is a large crystallite size as shown by the post-annealed sample at 200°C, resulting in low surface area as a result from a better morphology, thus an efficient charge extraction happened in the absorber layer. Therefore, a charge carrier can be transported and collected efficiently attributed to the reducing of charge recombination, thus producing a high current density and eventually give a better performance of device, as shown in Figure 7c and Figure 8d. We noticed that the current density of CBI cell is higher than the output voltage. Our result agrees well with the previous reported of [17] and [22]. Moreover, our current recorded value of current density is high than those mentioned references. In addition, it might be due to the CBI has a better optical and electronic properties [47].

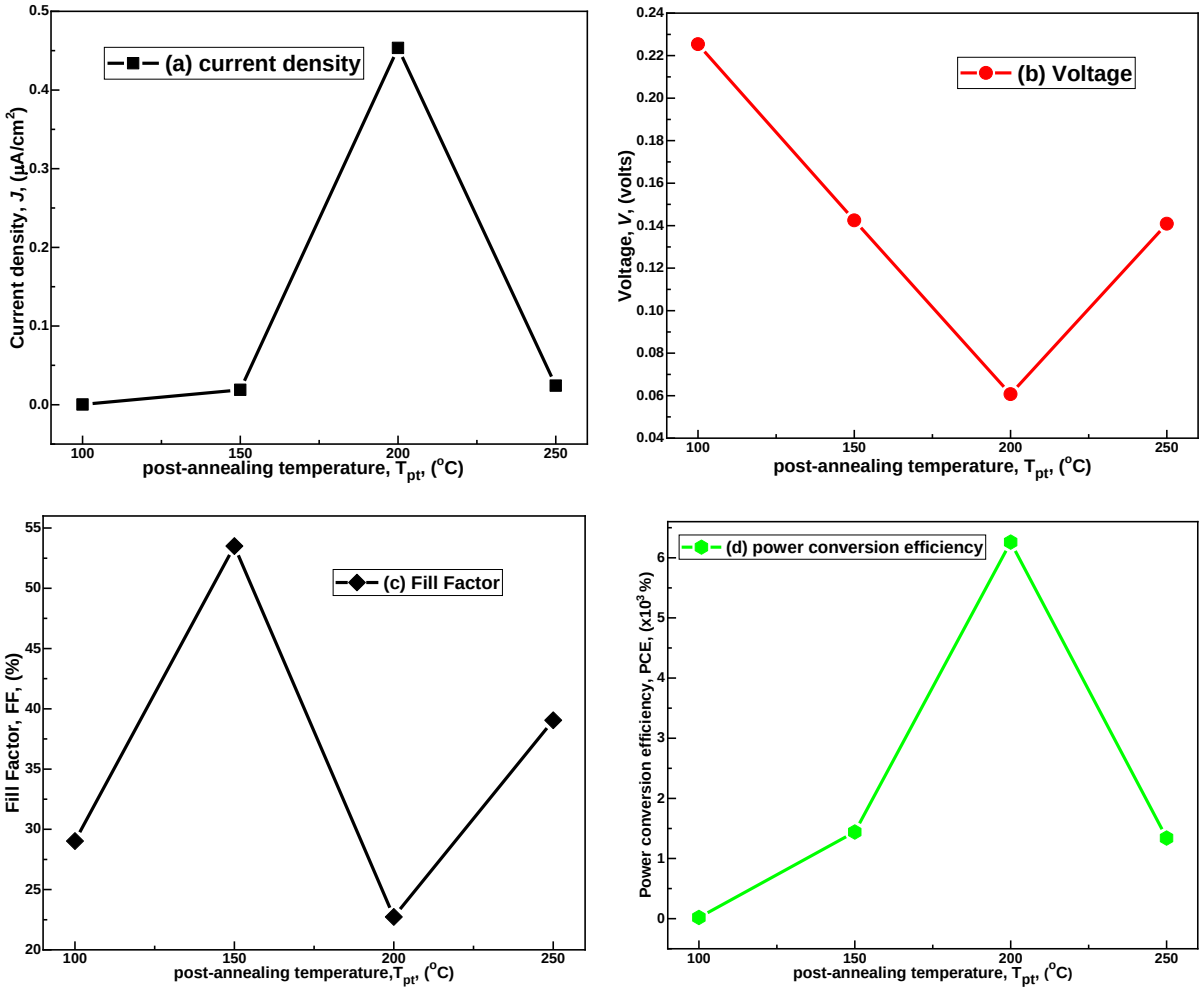

Figure 8. The graph of solar cell parameters of CBI films: (a) current density, (b) output voltage, (c) fill factor, and (d) device efficiency.

Furthermore, from Figure 8 we can observe that both parameter (J_{sc} and PCE) is having a similar trend of the graph. It means that the efficiency of CBI cells is relying on the current density as compared to two other parameters, particularly at 200°C, whereby the high value of current density is 0.45 mA/cm^2 much influencing the efficiency of CBI cells with the efficiency of 0.00626% as shown in Figure 8a and Figure 8d, respectively. In contrast with the voltage and fill factor, are contributing a more effect on the performance of CBI cells at 150°C and 250°C, which showing almost same value of voltage were 0.14249 V and 0.14088 V, and the fill factor values are 54% and 39%, respectively. It is higher than two post-annealing temperature, which is 100°C and 200°C, as shown in Figure 8b and Figure 8c, respectively, however, as discussed earlier, for 250°C of PAT is due to the deformation of CBI film (defect), while at 100°C of PAT is due to the very poor morphology attributed to high percentage of porosity, thereby producing a very poor efficiency as shown in Figure 8a.

In brief, larger grain size resulting from post-annealing temperature with less porosity and a small crystallite size are identified as three factors that might contribute to a better current density and efficiency values of the CBI cell device at 200°C. At the end, it can be summarized, particularly on the overall efficiency of four samples were still low. It might be due the effects of the thickness on the performance of CBI cell, which should be studied in the future for further improvement, since the CBI has a large crystal structure that might be affected the thickness of CBI film as an active absorber layer. Eventually, influencing the performance of the device. However, this effect is not clarified yet, and further investigation focusing on the film thickness effect is necessary in future. The higher efficiency of the state-of-the-art CBI based solar cell as ever reported is 3.20 % in last year [48].

CONCLUSION

The fabrication of CBI cells by using a simple HIM and changing the post-annealing temperature was demonstrated for the first time. Our studies showed that the post-annealing temperature strongly influences the film crystallinity, crystallite size, surface morphology, and optical properties of CBI PeSCs.

The post-annealing temperature was introduced effectively to improve the grain size, surface roughness, reduced the film porosity and optical bandgap. Hence enhances the crystalline and absorption properties of CBI films. Thus, leading to an increase in the current density and efficiency, which are 0.45 mA/cm^2 and 0.0063%, respectively, at 200^{o}C of post-annealing temperature. In addition, on increasing the annealing-temperature from 100^{o}C to 200^{o}C attributed to the better optical properties with a narrower indirect bandgap at extended wavelength absorption region. Therefore, it can be concluded that the changes in the structural, morphological, optical and electrical properties of the CBI PeSCs are strongly dependent on the post-annealing temperature. On the other hand, the HIM technique proposed in this work is a simple, saved precursor solution and an easy fabrication method to fabricate high crystallinity, compact and less porosity of Pb-free perovskites films. At the end, the fabrication of CBI PeSCs with HIM offered plenty of space to be explored and improved in future studies, such as testing of CBI-PeSCs with other alternative annealing temperatures and prolong the immersion temperatures.

ACKNOWLEDGEMENTS

The author would like to acknowledge the Universiti Teknologi MARA (UiTM) for financial and studies supports. Unforgettable acknowledge to the Japanese government for providing an expertise, facilities, knowledge and financial throughout this work.

REFERENCES

1. Waykar, R., Bhorde, A., Nair, S., Pandharkar, S. and Gabhale, B. (2020) Environmentally stable lead-free cesium bismuth iodide ($Cs_3Bi_2I_9$) perovskite: Synthesis to solar cell application. *J. Phys. Chem. Solids*, **146**, 109608.

2. Achoi, M. F., Kato, S., Kishi, N. and Soga, T. (2024) Improved photovoltaic properties of $((CH_3NH_3)_{1-x}Cs_x)_3Bi_2I_9$: (x = 0-1.0) hybrid perovskite solar cells via a hot immersion method. *AIMS Mater. Sci.*, **11**, 605–619.

3. Dehingia, A., Das, U. and Roy, A. (2021) Experimental and computational study on $Cs_3Bi_2I_9$ perovskite solar cell: A comparison of device performance. *Mater. Today Proc.*, **74**, 234–239.

4. Sanders, S., Stümmler, D., Pfeiffer, P., Ackermann, N., Simkus, G. and Heuken, M. (2019) Chemical Vapor Deposition of Organic-inorganic Bismuth-Based Perovskite Films for Solar Cell Application. *Phys. Status Solidi A*, **9**, 9774.

5. Shirahata, Y. (2020) Effects of annealing temperature on photovoltaic properties of lead-free $(CH_3NH_3)_3Bi_2I_9$ solar cells. *J. Ceram. Soc. Japan*, **128**, 298–303.

6. Momblona, C., Kanda, H., Sutanto, A. A., Mensi, M., Roldán-Carmona, C. and Nazeeruddin, M. K. (2020) Co-evaporation as an optimal technique towards compact methylammonium bismuth iodide layers. *Scientific Reports*, **10**, 10640.

7. Achoi, M. F., Aiba, S., Kato, S., Kishi, N. and Soga, T. (2021) Effect of Spinning Rate on the Performance of Multilayer Bi- perovskite Solar Cells. *Int. J. Nanoelectron. Mater.*, **14**, 1–10.

8. Jain, S. M., Phuyal, D., Davies, M. L., Li, M., Philippe, B., De Castro, C., Qiu, Z., Kim, J., Watson, T., Tsoi, W. C., Karis, O., Rensmo, H., Boschloo, G., Edvinsson, T. and Durrant, J. R. (2018) An effective approach of vapour assisted morphological tailoring for reducing metal defect sites in lead-free, $(CH_3NH_3)_3Bi_2I_9$ bismuth-based perovskite solar cells for improved performance and long-term stability. *Nano Energy*, **49**, 614–624.

9. Zhang, Y., Pathak, R., Zheng, D., Cheng, P., Chen, T., Chen, X., Wei, K., Wang, R. and Wu, F. (2022) Synthesis of cesium bismuth iodide perovskite using toluene as anti-solvent with higher photocurrent response. *Mater. Lett.*, **310**, 131514.

10. Ataei, M., Adelifard, M. and Hosseini, S. S. (2021) Physical Properties and Photovoltaic Performance of Perovskite Solar Cells Based on Lead-Free $A_3Bi_2I_9$ (A = CH_3NH_3, Cs) Active Layers. *J. Electron. Mater.*, **50**, 571–579.

11. Mohammad, T., Kumar, V. and Dutta, V. (2019) Electric field assisted spray coated lead free bismuth iodide perovskite thin film for solar cell application. *Sol. Energy*, **182**, 72–79.

12. Bresolin, B. M., Hammouda, Ben, S. and Sillanpää, M. (2019) Methylammonium iodo bismuthate perovskite $(CH_3NH_3)_3Bi_2I_9$ as new effective visible light-responsive photocatalyst for degradation of environment pollutants. *J. Photochem. Photobiol. A Chem.*, **376**, 116–126.

13. Mutlu, A., Yesil, T. and Zafer, C. (2021) Utilization of coordinating green solvents for high quality methylammonium bismuth iodide thin films for photovoltaic applications. *Org. Electron*, **95**, 106191.

14. Jain, S. M., Edvinsson, T. and Durrant, J. R. (2019) Green fabrication of stable lead-free bismuth based perovskite solar cells using a non-toxic solvent. *Commun. Chem.*, **2**, 1–7.

15. Zhang, H., Xu, Y., Sun, Q., Dong, J., Lu, Y., Zhang, B. and Jie, W. (2018) Lead free halide perovskite $Cs_3Bi_2I_9$ bulk crystals grown by a low

temperature solution method. *Cystal Eng. Commun*., **20**, 4935–4941.

16. Bai, F., Hu, Y., Qiu, T., Maio, X. and Zhang, S. (2018) Lead-free, air-stable ultrathin $Cs_3Bi_2I_9$ perovskite nanosheets for solar cells. *Olar Energy Mater. Sol. Cells*, **184**, 15–21.

17. Johansson, M. B., Zhu, H. and Johansson, E. M. J. (2016) Extended Photo-Conversion Spectrum in Low-Toxic Bismuth Halide Perovskite Solar Cells. *J. Phys. Chem. Lett*., **7**, 3467–3471.

18. Öz, S., Hebig, J. -C., Jung, E., Singh, T., Lepcha, A., Olthof, S., Flohre, J., Gao, Y., German, R., Loosdrecht, P. H. M. V., Meerholz, K., Kirchartz, T. and Mathur, S. (2016) Zero-dimensional $(CH_3NH_3)_3Bi_2I_9$ perovskite for optoelectronic applications. *Sol. Energy Mater. Sol. Cells*, **158**, 195–201.

19. Borriello, I., Cantele, G. and Ninno, D. (2008) Ab initio investigation of hybrid organic-inorganic perovskites based on tin halides. *Phys. Rev. B - Condens. Matter Mater. Phys*., **77**, 1–9.

20. Devasia, S., Shaji, S., Avellaneda, D., Aguilar Martinez, J. A. and Krishnan, B. (2022) In situ crystallization of 0D perovskite derivative $Cs_3Bi_2I_9$ thin films via ultrasonic spray. *J. Alloys Compd.*, **893**, 162294.

21. Qi, Z., X. Fu, T. Yang, D. Li, P. Fan, H. Li, F. Jiang, L. Li, Z. and Luo, X. Z. (2019) Highly stable lead-free $Cs_3Bi_2I_9$ perovskite nanoplates for photodetection applications. *Nano Res.*, **12**, 1894–1899.

22. Aiba, S., Achoi, M. F., Kato, S., Kishi, N. and Soga, T. (2023) Influence of Anti-Solvents on the Performance of Cesium Bismuth Iodide Perovskite Solar Cells. *Key Eng. Mater*., **951**, 105–114.

23. Achoi, M. F., Noman, M. A. A., Kato, S., Kishi, N. and Soga, T. (2021) Synthesis of bismuth triiodide nanofibers by spin-coating at room temperature. *Materialia*, **16**, 101077.

24. Lakhdar, N. and Hima, A. (2020) Electron transport material effect on performance of perovskite solar cells based on $CH_3NH_3GeI_3$. *Opt. Mater. (Amst).*, **99**, 109517.

25. Rhrissi, I., El Harafi, O., Arba, Y. and Moubah, R. (2023) Impact of film thickness on the structural and linear/nonlinear optical properties in highly oriented $Cs_3Bi_2I_9$ perovskite films. *Mater. Sci. Eng. B*, **297**, 116784.

26. Alanazi, T. I. (2023) Current spray-coating approaches to manufacture perovskite solar cells. *Results Phys.*, **44**, 106144.

27. Cai, H., Liang, X., Ye, X., Su, J., Guan, J., Yang, J., Liu, Y., Zhou, X., Han, R., Ni, J., Li, J. and Zhang, J. (2020) High efficiency over 20% of perovskite solar cells by spray coating via a simple process. *ACS Appl. Energy Mater*., **3**, 9696–9702.

28. Shahiduzzaman, Md., Hossain, M. I., Gantumur, M., Yue, F., Rafij, J. H., Akhtaruzzaman, Md., Nakano, M., Karakawa, M., Tomita, K., Nunzi, J. M. and Taima, T. (2024) Unlocking high stability in perovskite solar cells through vacuum-deposited $Cs_3Bi_2I_9$ thin layer. *Nano Energy*, **127**, 109726.

29. Sanders, S., Stümmler, D., Pfeiffer, P., Ackermann, N., Simkus, G., Heuken, M., Baumann, P. K., Vescan, A. and Kalisch, H. (2019) Chemical Vapor Deposition of Organic-Inorganic Bismuth-Based Perovskite Films for Solar Cell Application. *Sci. Rep*., **9**, 9774.

30. Achoi, M. F., Aiba, S., Kato, S., Kishi, N. and Soga, T. (2022) Fabrication and properties of compact $(CH_3NH_3)_3Bi_2I_9$ perovskite solar cell by the hot immersion method. *Optical Materials: X*, **15**, 100158.

31. Achoi, M. F., Aiba, S., Kato, S., Kishi, N. and Soga, T. (2021) A novel approach towards compact and improved-crystallinity methylammonium bismuth iodide film via hot immersion method. *Mater. Lett. X*, **16**, 100096.

32. Achoi, M. F., Kato, S., Kishi, N. and Soga, T. (2024) Annealing Time Dependence in the Fabrication of Bismuth-based Perovskite Solar Cells (Bi-PeSCs) by the Hot Immersion Method. *J. Mech. Eng*., **21**, 83–103.

33. Achoi, M. F. B, Asiah, M. N. bt, Rusop, M. and Abdullah, S. (2011) The Effect of Growth Temperature on the Surface Properties of TiO_2 Nanostructures Grown on TiO_2 Templates. *Trans. Mater. Res. Soc. Japan*, **36**, 273–279.

34. Matiur, R. M., Kato, S. and Soga, T. (2021) All-solution-processed environment-friendly solid-state BiOI photovoltaic cell with high-short-circuit current by successive ionic layer adsorption and reaction (SILAR). *J. Mater. Sci. Mater. Electron*, **32**, 18342–18350.

35. Clabel, J. L. H., Awan, I. T., Rivera, V. A. G., Nogueira, I. C., Silva, M. P. D., Li, M. S., Ferreira, S. O. and Marega, Jr. E. (2019) Growth Process and Grain Boundary Defects in Er Doped $BaTiO_3$ Processed by EB-PVD: A Study by XRD, FTIR SEM and AFM. *Appl. Surf. Sci.*, **493**, 982.

36. Clabel, J. L., Nazrin, S. N., Lozano, G., Silva, M. Pd., Li, M. S. and Marega, Jr. E. (2021) Activation Energy and its Fulctuations at Grain Boundaries of Er^{3+}: $BaTiO_3$ Perosvkite Thin Films:

Efect of Doping Concentration and Annealing Temperature. *Vacuum*, **194**, 110562.

37. Achoi, M. F., Aiba, S., Kato, S., Kishi, N. and Soga, T. (2023) Influence of Post-Annealing on the Properties of Methylammonium Bismuth Iodide Perovskite Solar Cells Through the Hot Immersion Method. *J. Electron. Mater.*, **52**, 351–367.

38. Abuelwafa, A., Matiur, R. M. D., Putri, A. A. and Soga, T. (2020) Synthesis, Structure, and Optical Properties of the Nanocrystalline Bismuth Oxyiodide (BiOI) for Optoelectronic Application. *Opt. Mater. (Amst).*, **109**, 110413.

39. Shargaieva, O., Lang, F., Rappich, J., Dittrich, T., Klaus, M., Meixner, M., Genzel, C. and Nickel, N. H. (2017) The influence of the grain size on the properties of CHNHPbI thin films. *ACS Appl. Mater. Interfaces*, **9**, 38428–38435.

40. Matiur, R. M. D., Abuelwafa, A. A., Putri, A. A., Kato, S., Kishi, N. and Soga, T. (2021) Annealing Effects on Structural and Photovoltaic Properties of the Dip-Silar-Prepared Bismuth Oxyhalides (BiOI, Bi_7O_9I3, Bi_5O_7I) films. *SN Appl. Sci.*, **3**, 1.

41. Shin, S. S., Correa Baena, J. P., Kurchin, R. C., Polizzotti, A., Yoo, J. J., Wieghold, S., Bawendi, M. G. and Buonassisi, T. (2018) Solvent-Engineering Method to Deposit Compact Bismuth-Based Thin Films: Mechanism and Application to Photovoltaics. *Chem. Mater.*, **30**, 336–343.

42. Lan, C., Luo, J., Zhao, S., Zhang, C., Liu, W., Hayase, S. and Ma, T. (2017) Effect of lead-free $(CH_3NH_3)_3Bi_2I_9$ perovskite addition on spectrum absorption and enhanced photovoltaic performance of bismuth triiodide solar cells. *J. Alloys Compd.*, **701**, 834–840.

43. Ran, C., Wu, Z., Xi, J., Yuan, F., Dong, H., Lei, T., He, X. and Hou, X. (2017) Construction of Compact Methylammonium Bismuth Iodide Film Promoting Lead-Free Inverted Planar Heterojunction Organohalide Solar Cells with Open-Circuit Voltage over 0.8 V. *Journal of Physical Chemistry Letters*, **8**, 394–400.

44. Matiur, R. M., Noman, M. A. A., Kato, S. and Soga, T. (2021) A novel modest synthesis of device applicable flakes based stable BiOI film by the oxidation of BiI_3 film. *Journal of Alloys and Compounds*, **873**, 159715.

45. Xiao, Z., Dong, Q., Bi, C., Shao, Y., Yuan, Y. and Huang, J. (2014) Solvent Annealing of Perovskite-Induced Crystal Growth for Photovoltaic-Device Efficiency Enhancement. *Adv. Mater.*, **26**, 6503–6509.

46. Ma, G. (1986) Solar Cells: Operating Principles, Technology and System Applications, Sydney. *UNSW Press*, 85–102.

47. Park, B. -W., Philippe, B., Zhang, X., Rensmo, H., Boschloo, G. and Johansson, E. M. J. (2015) Bismuth Based Hybrid Perovskites $A_3Bi_2I_9$ (A: Methylammonium or Cesium) for Solar Cell Application. *Adv. Mater.*, **9**, 6806–6813.

48. Masawa, S. M., Li, J., Zhao, C., Liu, X. and Yao, J. (2022) 0D/2D Mixed Dimensional Lead-Free Caesium Bismuth Iodide Perovskite for Solar Cell Application. *Materials (Basel)* **15**, 2180.

49. Eperon, G. E., Burlakov, V. M., Docampo, P., Goriely, A. and Snaith, H. J. (2014) Morphological Control for High Performance, Solution-Processed Planar Heterojunction Perovskite Solar Cells. *Adv. Funct. Mater.*, **24**, 151.